Nanosecond laser-induced surface coloration of 304 stainless steel simulation: integrating thin-film interference and additive color mixing principles with color space conversion and image processing techniques

Xu Peng[1] , Li Ming[1] , Zhang Huanzhen[1] *

1 College of Mathematical and Physical Sciences and Engineering, Hebei University of Engineering, Handan, Hebei 056000 , China;

Abstract

Nanosecond laser-induced surface coloration (NLISC) has attracted considerable research interest owing to its high precision, ease of automation, and environmental compatibility. However, optimization of the process parameters revealed a critical mismatch between theoretical predictions and experimental results. To this end, the current study developed a Python-based simulation system for NLISC of 304 stainless steel by integrating thin-film interference and additive color mixing principles with color space conversion and image processing techniques. The proposed system achieved closed-loop validation between theory and experiment. This study confirmed that thin-film interference serves as the primary physical mechanism for nanosecond laser-induced surface coloration on 304 stainless steel. Moreover, it provided a reliable predictive tool and methodology for further optimization and wider implementation of the NLISC technology.

Keywords: Nanosecond laser; Laser-induced surface coloration; Thin-film interference; Additive color mixing; Color space conversion

1. Introduction

Laser-induced surface coloration (LISC) has garnered considerable interest as a promising surface processing technique.[1]. This technique induces localized thermal excitation in the material through a high-energy-density laser beam, forming a colored oxide layer[2]. The resulting surface exhibits bright and stable coloration with minimal chromatic variation under fluctuating ambient temperature and humidity. Additionally, it demonstrates smooth topography, wear resistance, and exceptional fade resistance[3, 4]. Compared with conventional chemical coloration methods, LISC significantly reduces chemical reagent usage, thus mitigating environmental pollution and aligning with global sustainable manufacturing trends[5].

Despite significant advancements in the application of this technology, the underlying coloration mechanism remains incompletely elucidated and subject to ongoing debate. Three principal mechanisms have been proposed to explain laser-induced coloration on metallic surfaces:

(1) Laser-induced formation of an oxide layer, where coloration arises from thin-film interference[6];

(2) Laser-generated periodic surface structures producing color through diffraction principles[7];

(3) Plasmonic coloration induced by metallic nanoparticles and associated nanostructures[8]. Among these, the laser-induced oxide layer approach has emerged as the predominant method for metallic surface coloration, attributed to its advantages in processing speed, chromatic stability, and cost-effectiveness[9].

Numerous scholars globally have investigated laser-induced oxide layer coloration technology. Li et al.[10] employed a 355 nm UV solid-state laser for photothermal oxidation of 304 stainless steels, demonstrating that laser parameters significantly influence oxide layer structure and composition. Variations in scanning speed alter oxide layer morphology, while multiple scans increase film thickness and induce compositional changes. Ma et al.[11] utilized a 532 nm nanosecond pulsed laser on 304 stainless steels, revealing that scanning speed and spacing

critically affect surface morphology, oxide layer characteristics, and color stability. Through thin-film interference analysis, they measured film thickness across colored samples, verifying relationships between oxide layer thickness, coloration effects, and laser parameters. Swayne et al.[12] applied a 1064 nm Nd:YAG pulsed laser to 316L stainless steel, establishing that laser power, frequency, and scanning speed profoundly impact surface topography, oxide layer composition, and color properties. Using analysis of variance (ANOVA) modeling and elemental analysis, they elucidated intrinsic connections among laser parameters, oxide layer features, and chromatic performance. Zhang et al.[3] employed a 1064 nm Q-switched laser to achieve surface coloration on 304 stainless steel, systematically investigating nanosecond laser coloration mechanisms. Their results demonstrate that varying laser parameters significantly modulate oxide layer thickness and produce diverse surface colors under distinct parameter combinations. Furthermore, combined theoretical and numerical analysis elucidates thermal conduction's critical influence on oxide layer formation and chromatic manifestation. Awasthi et al.[13] employed a 1030 nm nanosecond MOPA pulsed fiber laser to achieve color marking on AISI 304 stainless steel, systematically investigating the role of oxide layers in nanosecond laser coloration. Their results demonstrate that varying laser parameters significantly modulates oxide composition and layer thickness, producing diverse surface colors under distinct parameter combinations. Furthermore, combined compositional and morphological analyses elucidate the influence of chromium versus iron oxides on surface topography and mechanical hardness. Lazov et al.[14] systematically investigated the influence of raster step, scanning speed, and frequency on surface roughness and color formation of AISI 304 stainless steel, establishing quantitative relationships between laser processing parameters and chromatic effects. Li et al.[15] provided a comprehensive review of laser-induced metal oxidation coloring technology, systematically summarizing the coloring mechanisms, material-dependent behaviors, and optimization strategies across different metallic substrates.

However, the actual coloration effect is influenced by multiple factors including oxide layer thickness, refractive index, and film uniformity. As a result, noticeable discrepancies remain between color predictions based solely on laser parameters and experimental measurements[16], limiting the ability to precisely regulate color variation. In recent years, several researchers have conducted modeling and simulation studies of laser-induced coloration and have verified the effectiveness of color-prediction models in this field. Xue et al.[17]investigated the laser-coloring mechanism of TC4 Ti alloy using a 1064 nm nanosecond fiber laser combined with SCOUT optical simulation. The results indicate that the single pulse energy density, by modulating the mixed film's composition ratio and thickness, changes the superposition of reflection and interference and thus produces different colors. Xue et al.[18] used a 1064 nm nanosecond fiber laser to study structural color generation, color mixing mechanisms, and prediction modeling on AISI 304 stainless steel. They found that laser marking parameters significantly affect the selection, stability, and rendering of primary and structural colors. Under different arrangement states of the primary color units, the mixed colors exhibit varying color differences, and a fully juxtaposed arrangement can effectively avoid the interference caused by overlapping. In constructing the color prediction model, the adjustment of the correction factor w and the curvature parameter b affects the prediction accuracy for mixed colors. Ultimately, based on the proposed model, continuous-tone images can be achieved through laser coloring. Geng et al.[19] employed a 1064 nm nanosecond laser, combined with a BP (back-propagation) neural-network-based color-stability evaluation model, to investigate the color stability of laser color marking on Ti6Al4V titanium alloy and SS 304 stainless steel via coupled experiments and numerical simulations. The results indicate that barcode parameters and laser scanning speed significantly influence color stability and the surface temperature distribution; moreover, at different scanning speeds, color stability exhibits periodic fluctuations that correlate with the relative temperature difference.

To overcome the limitations of color prediction based solely on laser parameters and to evaluate the applicability of thin-film interference theory, This article developed a Python-based coloration simulation system. By comparative analysis of simulation and experimental results, This article elucidated the mechanistic role of thin-film interference in nanosecond laser-induced surface coloration (NLISC) on 304 stainless steel, establishing theoretical foundations for subsequent process parameter optimization and mechanism exploration.

2. Experimental Materials and Methodology

2.1 Materials

304 stainless steel is extensively utilized across multiple fields owing to its cost-effectiveness, exceptional corrosion resistance, favorable mechanical properties, and superior manufacturability, establishing it as the preferred substrate for LISC[20, 21]. For this experiment, we selected 1 mm-thick 304 stainless steel plates measuring 20 mm×20 mm with unidirectionally ground surfaces as the coloration substrate. The detailed chemical composition and physical properties[22-24] of the 304 stainless steel samples used in the experiments are listed in **Tables 1** and **2**, respectively:

Table 1. Chemical composition of 304 stainless steel (mass fraction, %)

Fe	Cr	Ni	Mn	Si	C	P	S
69.865	18	9	2	1	0.07	0.035	0.03

Table 2. Physical properties of 304 stainless steel

Melting point	Specific heat capacity	Density	Thermal conductivity	Reflectivity
1713 K	0.5 KJ/(kg·K)	7.93 g/cm^3	15 W/(m·K)	0.59

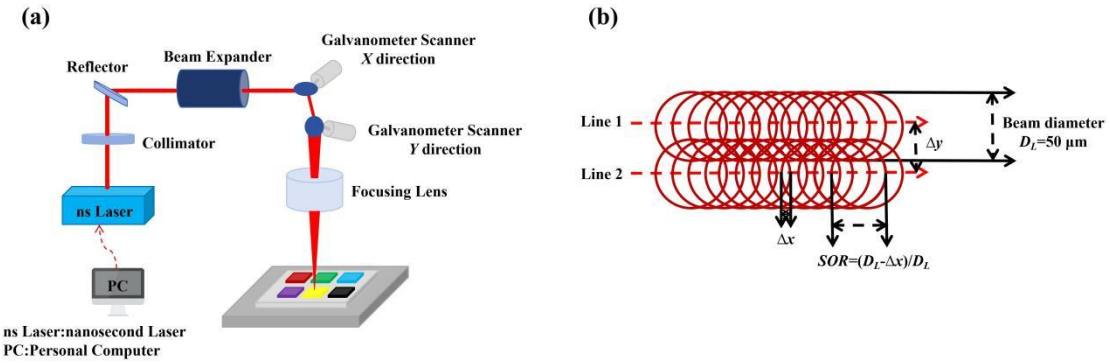

Fig. 1. Schematic diagrams: (a) NLISC experimental setup; (b) laser scanning path

2.2 Experimental Methodology

The experimental setup of the nanosecond-pulsed laser coloring system is shown in **Fig. 1(a)**. The system primarily consists of an IPG fiber laser, beam delivery optics, a galvanometer scanning system, an F-Theta focusing lens, a precision positioning stage, and a motion controller. The GAUTEK laser micromachining machine produced by Gauss Optical Grid (Beijing) Technology Co., Ltd. was used. The laser has a wavelength λ of 1064 nm, a rated power of 20 W, and a focused spot diameter of 50 μm. The pulse width τ_L can be set to 4, 8, 14, 20, 30, 50, 100, or 200 ns; the repetition frequency ranges from 20 to 2000 kHz; and the scanning speed ranges from 20 to 4000 mm/s.

The laser scanning path, illustrated in **Fig. 1(b)**, employed a bidirectional filling strategy: first, the focused beam scanned left to right horizontally, then scanned right to left at the preset filling spacing. This process was iterated until the designated area was fully filled.

The laser parameters chosen for this experiment were primarily selected based on preliminary trials and the parameter ranges reported in previous studies[14]; [25] on nanosecond-laser coloration of stainless steel. These parameter combinations have been shown to effectively induce oxidation reactions on the surface of 304 stainless steel and to produce visible thin-film colors. Using a controlled-variable approach, the scanning speed was varied while keeping the laser power, pulse repetition frequency, and pulse width constant. Adjusting the scanning speed consequently altered the spot overlap ratio (SOR), which determined the number of pulses received at the same location (N_p), thereby enabling regulation of the oxidation degree of the metal surface layer. To induce a richer and more continuous range of color variations, a small scanning-speed increment of 20 mm/s was selected, resulting in a scanning-speed range from 20 mm/s to 800 mm/s and a corresponding SOR range from 99.6% to 84%. Under these conditions, a continuous color transition from black to pale yellow was obtained, along with vivid intermediate hues such as gray, green, violet, blue, brown, and orange.

The NLISC experiments were conducted on 304 stainless steel surfaces under ambient temperature and atmospheric conditions. Pre-experimental preparation involved immersing samples in anhydrous ethanol for 3 min of ultrasonic cleaning to remove surface contaminants, followed by drying with oil-free compressed air and fixation on the laser processing stage. Key parameters were maintained as follows: laser power P_0 = 6 W, repetition frequency f_L = 100 kHz, pulse width τ_L = 200 ns, and spot diameter D_L = 50 μm. Scanning speed was systematically varied from 20 to 800 mm/s in 20 mm/s increments, corresponding to spot overlap ratio reductions from 99.6% to 84%. The beam spot overlap ratio (*SOR*) and line overlap ratio (*LOR*) were defined as follows:

$$SOR = (D_L - \Delta x) / D_L \tag{1a}$$

$$LOR = (D_L - \Delta y) / D_L \tag{1b}$$

where Δx is the spot distance, Δy is the line distance (see **Fig.1b**).

Post-experimental processing repeated ultrasonic cleaning and blow-drying procedures for all samples to eliminate residual contaminants.

3. Experimental Results

A total of 40 sets of experimental parameters were generated according to the aforementioned experimental procedure, and the resulting surface coloring effects on 304 stainless steel are collectively presented in **Fig. 2.**

The color evaluation of the experimental samples was conducted by photographing them under a standard illumination source. To ensure measurement accuracy, all imaging conditions

were kept consistent prior to subsequent color analysis. Color samples were arranged left-to-right and top-to-bottom, exhibiting a chromatic sequence of black, gray, green, violet, blue, brown, orange, and yellow. During nanosecond laser irradiation of 304 stainless steel surfaces, localized heating induced oxidation reactions that form an oxide layer. At elevated spot overlap ratio, increased effective pulses per unit area enhanced energy accumulation, thereby increasing oxide layer thickness[26]. Conversely, reduced overlap ratios diminished deposited pulses and energy accumulation, decreasing oxide layer thickness. Per thin-film interference principles, varying oxide layer thickness mediated wavelength-specific interference amplification or attenuation, thereby generating diverse surface colors[27]. Six specimens exhibiting pronounced chromatic characteristics were selected from the 40-color matrix for parametric analysis, with experimental details presented in **Table 3**.

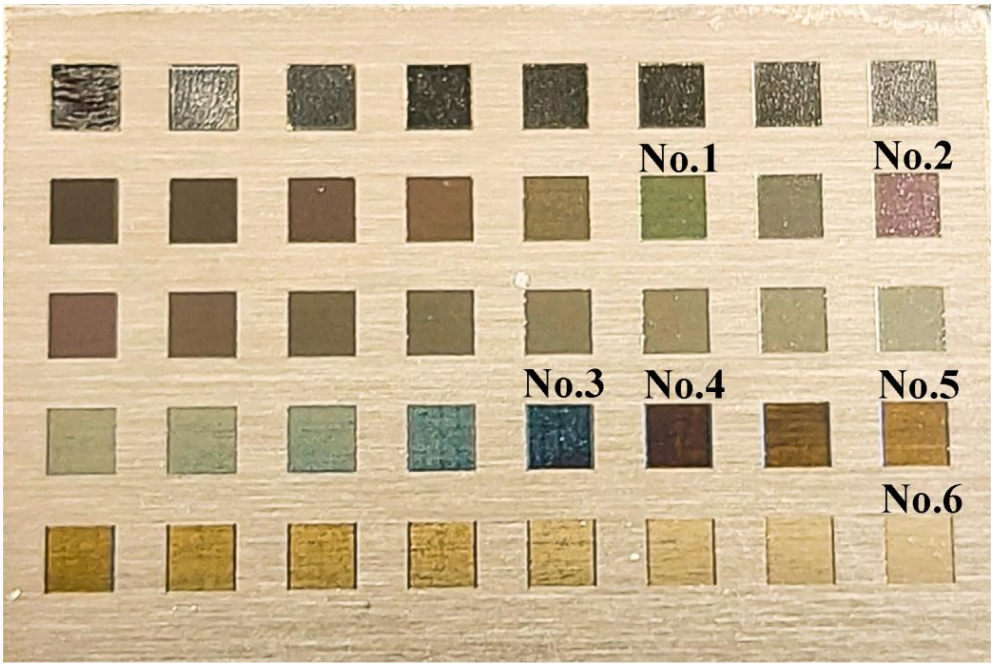

Fig. 2. The coloring effects on the 304 stainless steel surface

Table 3. Comparative analysis of experimental parameters for characteristic color patches

Field number	Color	Photo of surface	Scanning speed (mm/s)	Line spacing (μm)	SOR (%)
No.1	Green		280	2.8	94.4
No.2	Violet		320	3.2	93.6
No.3	Blue		580	5.8	88.4
No.4	Brown		600	6	88
No.5	Orange		640	6.4	87.2
No.6	Yellow		800	8	84

4.Thin-Film Interference & Additive Color Mixing Principles

4.1 Thin-Film Interference (TFI) Principle

During nanosecond laser irradiation of 304 stainless steel surfaces, high-energy-density laser beams induce localized oxidation reactions between the metal substrate and ambient oxygen, forming a uniform oxide layer[28]. When natural light impinges upon an oxide layer of thickness d, a portion of incident light transmits through the oxide layer, reflects at the oxide-substrate interface, and refracts outward, while another portion reflects directly at the air-oxide interface. When these reflected beams interfere, differential optical path lengths generate phase differences that produce constructive or destructive interference.This wavelength-selective amplification or attenuation yields interference colors corresponding to specific layer thicknesses[29].

Figure 3 illustrates the thin-film interference (TFI) schematic.

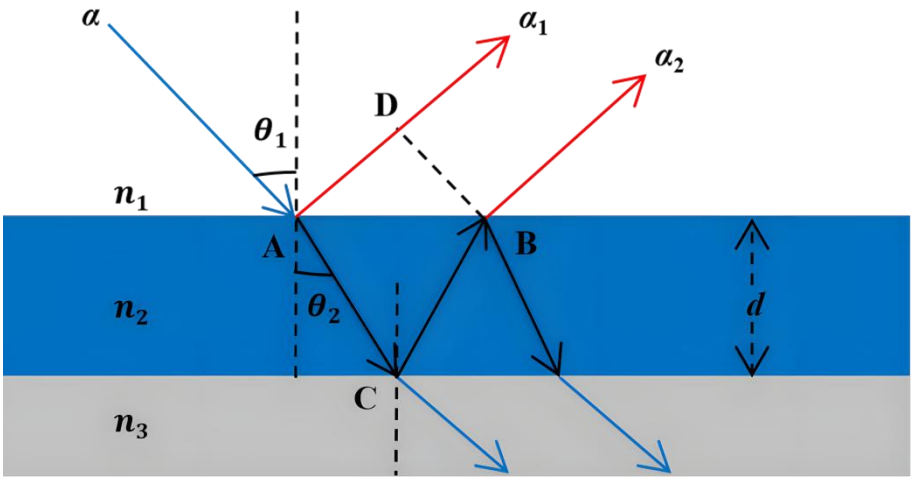

Fig. 3. Schematic diagram of the TFI theory principle

To ensure that the two emergent parallel beams α_1 and α_2 intersect, a converging lens is typically placed behind the thin film. According to Fermat's principle, the optical paths of all rays between the object and image points are equal; therefore, inserting a lens into the optical path does not introduce any additional phase difference. Consequently, from the transmission point B of beam α_2 on the upper surface of the thin film, a perpendicular line is drawn to beam α_1, with the foot of the perpendicular denoted as D. In this configuration, all rays in the plane containing BD have equal optical path lengths to the image point.

As shown by the geometrical analysis, the incident beam α is divided into two beams, α_1 and α_2 at the incident point A,and these two beams propagate along different paths. Owing to the difference in propagation distances, an optical path difference (Δ') arises between the two beams, which can be expressed as follows:

$$\Delta' = n_2(AC + CB) - n_1 AD \tag{2}$$

where n_1 denotes the refractive index of air, n_2 is the refractive index of the oxide layer.

In addition to the optical path difference caused by the difference in propagation paths, it is also necessary to consider whether a half-wave loss occurs for the reflected light relative to the incident light during reflection at the interfaces. According to the condition for the occurrence of half-wave loss, when reflection of the incident light at an interface occurs from an optically less dense medium to an optically denser medium, the reflected light experiences a half-wave loss relative to the incident light.Therefore, for the case shown in **Fig. 3**, the refractive index of the film is n_2, the refractive index of air is n_1, and points A and C are the reflection points.When $n_2 > n_1$, a half-wave loss occurs at point A, while no half-wave loss occurs at point C;When $n_2 < n_1$, no half-wave loss occurs at point A, while a half-wave loss occurs at point C. In general, if only one of the beams α_1 and α_2 experiences a half-wave loss relative to the incident beam, an additional optical path difference of $\lambda/2$ is introduced between the two beams. At this time, the optical path difference (Δ) between the two beams can be expressed as:

$$\Delta = \Delta' + \lambda/2 = n_2(AC + CB) - n_1 AD + \lambda/2 \tag{3}$$

For a thin film with thickness d, the incident angle and the refraction angle are denoted as θ_1 and θ_2, respectively. The geometrical relationships among AD, AC, CB, and AB satisfy:

$$\begin{aligned} AD &= AB\sin\theta_1 \\ AC &= CB = d/\cos\theta_2 \\ AB &= 2d\tan\theta_2 \end{aligned} \tag{4}$$

By applying Snell's law given in equation (5), the optical path difference for thin-film interference can ultimately be obtained as a function of the incident angle or refraction angle and the film thickness, as shown in equation (6). When the optical path difference is an even multiple of half a wavelength, constructive interference occurs between the two beams; when the optical path difference is an odd multiple of half a wavelength, destructive interference occurs. Consequently, bright and dark

regions are formed, respectively.

$$n_1 \sin\theta_1 = n_2 \sin\theta_2 \tag{5}$$

$$\begin{aligned}\Delta &= 2dn_2\cos\theta_2 + \frac{\lambda}{2} \\ &= 2d\sqrt{n_2{}^2 - n_1{}^2\sin{}^2\theta_1} + \frac{\lambda}{2} \\ &= \begin{cases} m\lambda, (m = 1,2,\ldots) \\ (2m+1)\lambda/2, (m = 0,1,2,\ldots) \end{cases}\end{aligned} \tag{6}$$

where m is an integer representing the interference order, and λ is the wavelength of the incident light, with the unit of nm.

From equations (6), the wavelength λ for constructive interference satisfies the following condition:

$$\lambda = \frac{4n_2 d\cos\theta_2}{2m-1} \tag{7}$$

Under normal incidence, where $\theta_1 = 0°$, the refraction angle becomes $\theta_2 = 0°$. Therefore, $\cos\theta_2 = 1$.Substituting this condition into equations (7), the relationship between the wavelength of the constructively interfering light and the corresponding parameters can be simplified as follows:

$$\lambda = \frac{4n_2 d}{2m-1} \tag{8}$$

The interference equation determines the wavelength λ of constructively interfering light through the oxide layer thickness d, refractive index n_2, and interference order m, thereby establishing the corresponding chromatic manifestation.

However, in TFI processes, incident light of different wavelengths generates distinct interference spectra under identical oxide layer thickness and incidence angles[30]. Under white light illumination, multiple wavelengths λ simultaneously satisfy constructive interference conditions. The resulting chromatic manifestation constitutes composite coloration derived from polychromatic superposition[31].For visible light (400-760 nm wavelength range), given known oxide layer thickness d and refractive index n_2, the constructive interference condition is solved within the visible spectrum to identify valid interference orders m. The corresponding wavelengths are computed, and additive color mixing principles[32] are applied to synthesize the composite interference coloration.

The quantitative framework relating oxide layer thickness d, refractive index n_2, and constructive interference wavelengths provides fundamental theoretical support for simulating NLISC on 304 stainless steel. Within the developed simulation system, input parameters d and n_2, enable computation of interference wavelengths via equation (8), facilitating predictive chromatic visualization of TFI effects. This methodology achieves comprehensive simulation of NLISC processes.

The above derivation assumes that the substrate (304 stainless steel) is a perfectly transparent dielectric medium. In reality, the substrate is a metal with a complex refractive index $\tilde{n} = n - ik$,where k is the extinction coefficient. At the oxide/metal interface, the reflection phase shift is not strictly 0 or π as in the dielectric case, but rather a wavelength-dependent value determined by the optical constants of both the oxide layer and the metal substrate. A rigorous treatment would require the use of complex Fresnel coefficients. In the current simulation system, This article have adopted the conventional thin-film interference model for dielectric films on an absorbing substrate, which approximates the phase shift at the oxide/metal interface as π under the assumption that the metal is highly reflective and the oxide thickness is much smaller than the penetration depth of light. This approximation is widely used in the literature for laser-induced oxide coloration. However, this is indeed only a simplification; future work will incorporate the full complex refractive index of 304 stainless steel to refine the model.

4.2 Additive Color Mixing Principle

The CIE Lab* color model, established by the International Commission on Illumination (CIE), is an internationally standardized system for color quantification. It is derived from the CIE 1931 XYZ color space. It uses tristimulus values, which describe a color by the amounts of three primary colors (red, green, and blue) that, when combined additively, produce a visual match for that color. Based on human visual response characteristics, this device-independent model comprehensively describes perceptible colors without reliance on specific light sources or materials[33]. The model characterizes color through three fundamental parameters L^*, a^*, and b^*, where L^* is the lightness gradient while a^* and b^* are chromatic components. Notably, L^* ranges from 0 to 100, representing the black-to-white lightness gradient; a^* spans from -128 to 127, describing the green-to-red chromatic variation; b^* spans from -128 to 127, representing the blue-to-yellow chromatic variation[34]. The CIELAB color space schematic is presented in **Fig. 4:**

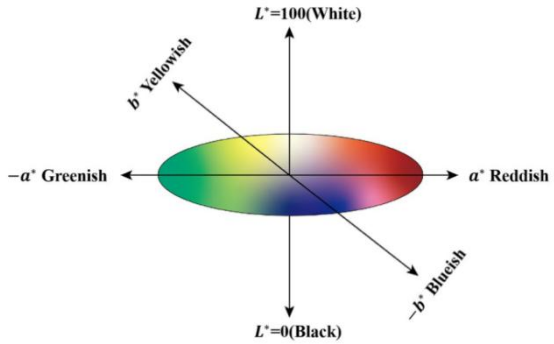

Fig. 4. CIELAB color space schematic diagram

For monochromatic radiation of wavelength λ, the XYZ tristimulus values are calculated using the CIE standard observer color-matching functions. Spectral reflectance measured under CIE standard illuminant is converted to corresponding tristimulus values via Eq. (9)[35]:

$$\begin{aligned} X &= k\sum_{\lambda}\bar{x}(\lambda)R(\lambda)S(\lambda)\triangle\lambda \\ Y &= k\sum_{\lambda}\bar{y}(\lambda)R(\lambda)S(\lambda)\triangle\lambda \\ Z &= k\sum_{\lambda}\bar{z}(\lambda)R(\lambda)S(\lambda)\triangle\lambda \end{aligned} \tag{9}$$

where

$$k = \frac{100}{\sum_{\lambda}\bar{y}(\lambda)S(\lambda)\triangle\lambda} \tag{10}$$

In Eq. (10), $\bar{x}(\lambda)$, $\bar{y}(\lambda)$, $\bar{z}(\lambda)$ denote the spectral tristimulus values, quantifying the human eye's relative spectral sensitivity to red, green, and blue primaries, respectively; $S(\lambda)$ represents the relative spectral power distribution of the CIE standard illuminant; $R(\lambda)$ constitutes the spectral reflectance measured under CIE standard illuminant D55 at a 2° observation geometry. Consequently, monochromatic spectral data are mapped to corresponding XYZ tristimulus values and subsequently transformed into the CIELAB color space via equation (11), establishing a bijective mapping between tristimulus values and coordinates[35].

$$\begin{cases} L^* = 116f\left(\dfrac{Y}{Y_n}\right) - 16 \\ a^* = 500\left[f\left(\dfrac{X}{X_n}\right) - f\left(\dfrac{Y}{Y_n}\right)\right] \\ b^* = 200\left[f\left(\dfrac{Y}{Y_n}\right) - f\left(\dfrac{Z}{Z_n}\right)\right] \\ f(t) = \begin{cases} \sqrt[3]{t} & t > e \\ \dfrac{k\bullet t + 16}{116} & \mathrm{t} \le \mathrm{e} \end{cases} \end{cases} \tag{11}$$

where the constants are e≈0.008856 and k≈903.3[36], and the CIE standard illuminant D55 reference white coordinates are X_n=95.68, Y_n=100, Z_n=92.15[34].

Within the TFI model, the surface oxide layer may exhibit interference enhancement at multiple wavelengths. The spectral components of the interference-enhanced light significantly govern human color perception. To accurately simulate polychromatic superposition effects, additive color mixing principles must be applied[37]. The foundational principle states that intensity responses from distinct interference wavelengths undergo linear superposition, thereby replicating the human eye's psychophysical response to composite light[38]. In the CIE XYZ color space, the net tristimulus value from polychromatic interference is expressed as follows:

$$X = \sum_{i=1}^{n} X_i, Y = \sum_{i=1}^{n} Y_i, Z = \sum_{i=1}^{n} Z_i \tag{12}$$

where X_i, Y_i, and Z_i denote the tristimulus components for each interfering wavelength, which linear superposition accurately simulates additive color mixing. This criterion aligns with the linear psychophysical response of the human visual system to polychromatic light intensities, enabling precise simulation of interference color blending. The simulation system employs the CIELAB color space to approximate additive color mixing principles:

$$L = \sum_{i=1}^{n} L_i, a = \sum_{i=1}^{n} a_i, b = \sum_{i=1}^{n} b_i \tag{13}$$

where L^*_i, a^*_i and b^*_i represent the CIELAB coordinates for each interfering wavelength; the system applies additive color mixing principles through linear summation of these components. This methodology accurately simulates comprehensive human chromatic perception under multi-wavelength interference conditions[39], ensuring that simulated results fully capture multi-wavelength color blending characteristics.

To establish a direct link between the theoretical model and experimental validation, the constructive-interference wavelengths calculated from the thin-film interference model were converted into the corresponding thin-film colors, and the final simulated colors were obtained via the additive color-mixing principle. These simulated colors were then matched one-to-one with the experimental color patches produced at different scanning speeds, enabling a direct comparison between theoretical predictions and experimental results.

5. System Design and Implementation

To verify the predictive capability of thin-film interference theory for nanosecond-laser coloration and to achieve a visualized mapping from physical parameters to perceived colors, this study develops a simulation system that integrates thin-film interference and additive color-mixing principles with color-space conversion and image-processing techniques. The system adopts a decoupled front-end/back-end architecture to ensure computational independence of the model and accessibility of the results, providing an efficient and visualized tool for color validation. The core system consists of three functional modules: a thin-film-interference-based color simulation module, a color-space conversion module, and an experimental image analysis module. The back-end algorithms are implemented in Python, leveraging its scientific-computing libraries for physical calculations and color transformations, while the front-end interface is built using Web technologies to facilitate seamless integration among user interaction, data processing, and image interpretation.[40].

5.1 System Entry and Functional Navigation

The system's welcome interface serves as the primary entry point and is designed to intuitively guide users toward the two core research functions. Through this interface, users can choose to enter either the "Color Simulation" module or the "Experimental Image Analysis" module. The interface emphasizes clarity and usability by providing explicit navigation options, enabling users to quickly access the desired module to perform color prediction or extract experimental data, thereby ensuring a smooth research workflow. The design of the welcome interface for system entry and function navigation is shown in **Figure 5.**

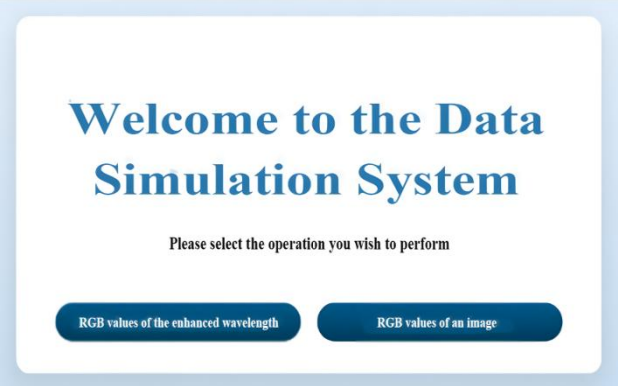

Fig. 5. System enter and function navigation interface

5.2 Input and Submission of Physical Parameters

The input interface provides users with a platform for configuring the simulation parameters required for thin-film interference. It is designed to allow the user to enter the key physical quantities needed for the thin-film interference model, namely the oxide-film thickness and refractive index. These parameters are used to solve the interference equations, thereby supporting the calculation of interference wavelengths and their corresponding RGB values based on thin-film interference theory and color-space conversion. The interface ensures the validity of the input data and reliably transmits these parameters to the back-end computation engine, supplying the necessary data acquisition and processing support for the subsequent interference-color simulation module. This design enables the full simulation workflow from physical parameters to the resulting color space. The layout of the input interface, which allows users to enter and submit physical parameters, is presented in **Figure 6**.

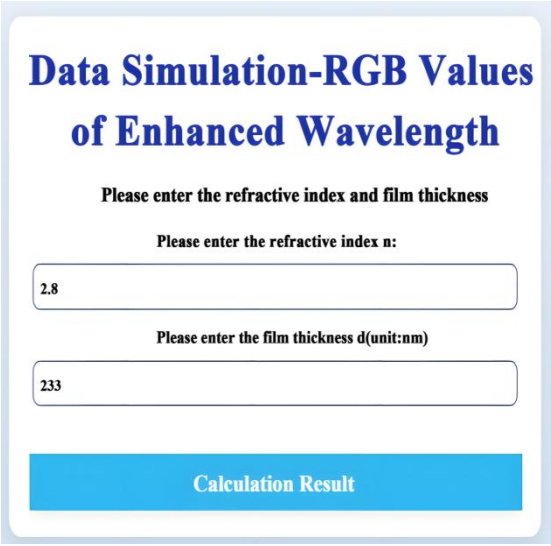

Fig. 6. Physical parameter input and submission interface

5.3 Simulation Results and Visualization

The calculation results interface presents theoretical predictions visually, facilitating direct comparison with experimental samples. The backend computations, implemented using Python scientific libraries, perform conversions between the RGB and CIE Lab* color spaces and carry out additive color mixing[41]. This workflow not only preserves the rigor of the theoretical derivations but also accurately simulates the superposition of multiple-order interference wavelengths through additive mixing. The interface presents the RGB values for each interference order, the corresponding CIE Lab* chromaticity values, and the final composite color derived from additive mixing principles. By organizing the data into distinct sections and incorporating color swatches for real-time preview, the interface effectively links numerical values with perceived colors. This comprehensive visualization allows users to clearly grasp the formation mechanisms of interference colors and to directly evaluate the agreement between simulated and experimental results. The calculation results page, used to visualize and compare simulation outputs, is illustrated in **Figure 7.**

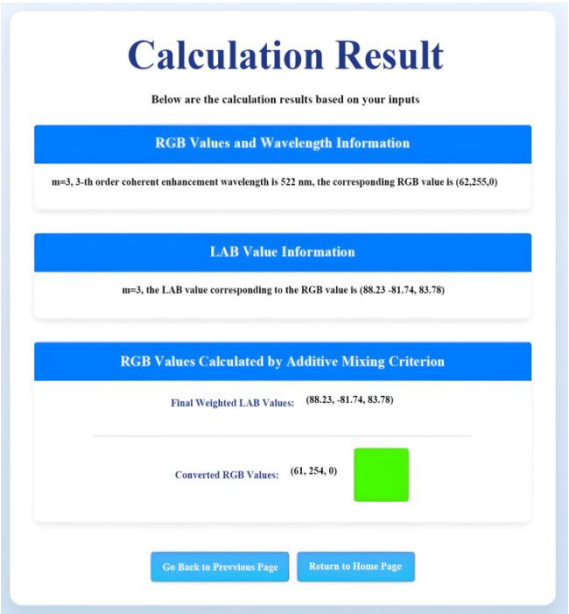

Fig. 7. Simulation results visualization and comparison interface

5.4 Quantitative Acquisition and Analysis of Experimental Colors

To enable direct validation, the interface extracts RGB values from experimental images and provides quantitative color measurements. Sample images are captured under a D55 standard illuminant to minimize ambient light interference. Users can interactively select specific regions of interest, while the system records coordinates in real time and overlays red dashed boxes with region labels for visual feedback. For each selected rectangular area, the mean values of the R, G, and B channels are automatically computed, reducing pixel-level noise[42].Repeatability tests demonstrate that the relative error of RGB values remains within ±2%, ensuring reliable statistical accuracy and enabling quantitative color comparison. This functionality effectively converts observed experimental phenomena into measurable data, serving as a critical link between simulation and experimental validation. The layout of the interface for quantitative extraction of experimental colors through image-based RGB value reading is shown in **Figure 8.**

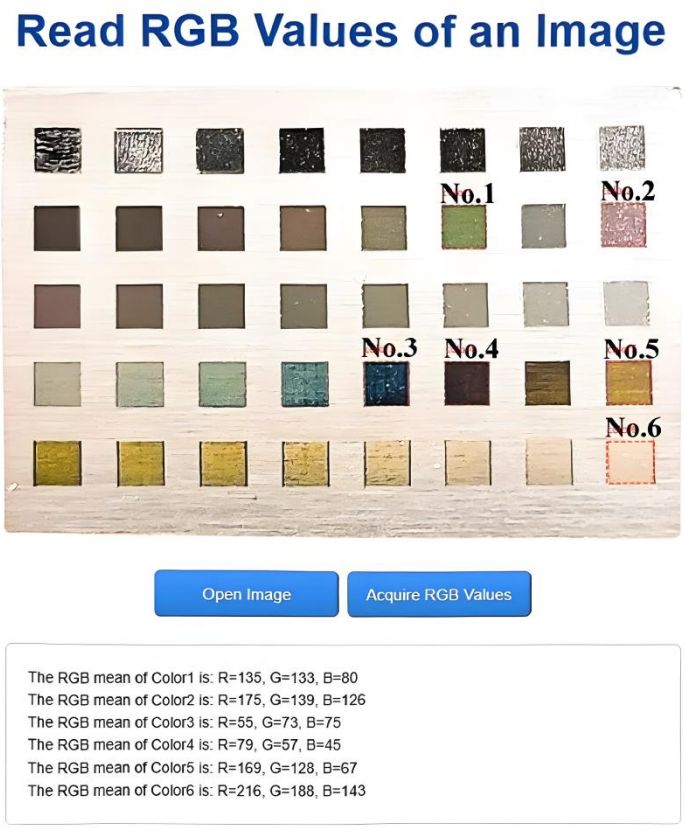

Fig. 8. Experimental color quantitative extraction interface

6. Data Simulation and System Verification

The core parameter governing TFI color formation is the oxide layer thickness *d*. Variations in film thickness directly alter the optical path difference of reflected light, thereby regulating the wavelength ranges for constructive or destructive interference, which ultimately yields distinct interference colors on the surface[43]. The interference wavelength sequences calculated from the theoretical model serve as the basis for determining the colors generated within the simulation system. In experiments, the overlap of laser spots is adjusted by varying the scanning speed, thereby controlling changes in the oxide film thickness to correspond with the thickness range defined in the predictive model. By matching parameters at this level, the color outputs from the simulation system can be directly compared with those of actual experimental samples, providing mutual validation between theoretical derivations and experimental observations.

To establish the physical relationship between oxide layer thickness *d* and the resulting coloration, based on equation (8), equation (14) can be obtained through transformation, and the corresponding relationship between film thickness and color can be obtained through simulation calculations. The formula used to simulate and calculate the oxide film thickness *d* is given as follows:

$$d = \frac{(2m-1)\lambda}{4n_2} \tag{14}$$

where λ is the wavelength of the incident light, with the unit of nm, m is an integer denoting the interference order, and n_2 is the refractive index of the oxide layer.

The refractive index of the oxide film is a key parameter in the simulation system. According to X-ray diffraction analysis, the oxide layer formed on the surface of 304 stainless steel by nanosecond laser irradiation primarily consists of Fe_2O_3[25].

Therefore, in this study, a refractive index of n_2=2.8 was selected, which falls within the range of refractive index values for Fe_2O_3 in the visible spectrum reported in the literature[44]. It is important to note that the refractive index of metal oxides such as Fe_2O_3 exhibits wavelength dispersion across the visible spectrum (400-760 nm), meaning that the refractive index changes as a function of the wavelength of light. The use of a constant refractive index is a simplification adopted in the current model. This assumption may introduce minor shifts in the theoretically predicted constructive interference wavelengths, but it does not affect the overall trend or the predictive capability of the simulation system for color sequence generation. The potential influence of dispersion is acknowledged as a limitation of the present study and will be addressed in future work by incorporating wavelength-dependent refractive index data. Within this computational framework, film thickness d was decremented from 300 nm in 1 nm steps to elucidate correlations between thickness, interference wavelengths, and resulting colors. At d=223 nm, an interference wavelength of λ=500 nm generated a simulated green hue. At a film thickness of d=203 nm, dual interference wavelengths λ_1=455 nm and λ_2=758 nm collectively generates a simulated violet color. For film thicknesses of 125, 55, 53, and 51 nm, the corresponding interference wavelengths measured 467, 616, 594, and 571 nm, yielding simulated colors of blue, brown, orange, and yellow respectively.

A reduction in spot overlap ratio substantially diminishes both the pulse deposition energy per unit area and the thermal accumulation effect, thereby limiting oxidation reactions and thinning the oxide layer thickness[45, 46]. In the experiments, increasing the laser scanning speed reduced the overlap ratio of laser spots from 94.4% to 84%, which weakened the pulse energy deposition per unit area and the associated thermal accumulation. This directly controlled the growth of the surface oxide film, resulting in a gradual thinning of the film. According to Equation (8), under normal incidence and a fixed refractive index, the constructive interference wavelength λ is proportional to the film thickness d. Consequently, based on thin-film interference effects, the decreasing film thickness directly alters the dominant interference wavelength, enabling the sequential formation of green, violet, blue, brown, orange, and yellow interference colors.

Comparisons between the experimentally produced colors and those simulated by the system show that variations in illumination, imaging angle, and potential microstructures on the material surface can influence light absorption and reflection, resulting in differences in brightness and color depth. As a result, the experimental colors do not perfectly match the simulated results. Nevertheless, the core value of the simulation system lies in its ability to predict and reproduce the sequence of color changes observed experimentally. This validates the predictive capability of the thin-film interference-based simulation system for color formation on nanosecond-laser-treated 304 stainless steel surfaces and reproduces the composite color characteristics arising from multi-wavelength interference, thereby demonstrating the reliability of the model. A systematic comparison between the experimental and simulated results for six representative colors is provided in **Table 4**.

Table 4. Comparison of simulated and experimental colors

Field number	Color	Experimental color image	Simulated color image	Interference wavelength λ (nm)	Simulated thickness d (nm)	simulated RGB values	ΔE
No.1	Green			500	223,...	(0,255,152)	35.9
No.2	Violet			455、758	203,...	(254,91,255)	34.3
No.3	Blue			467	125,...	(0,153,254)	38.4
No.4	Brown			616	55,...	(156,81,0)	22.1
No.5	Orange			594	53,...	(218,180,0)	19.8
No.6	Yellow			571	51,...	(228,254,0)	26.3

To quantitatively evaluate the agreement between the simulated and experimental colors, the color difference ΔE was calculated using the CIEDE2000 formula, which is the current CIE standard for industrial color difference evaluation. The experimental LAB values were derived from the RGB values extracted from the sample images, and the simulated LAB values were obtained directly from the thin-film interference model combined with additive color mixing. The calculated ΔE values for the six representative color patches are listed in the last column of Table 4. The calculated ΔE values range from

approximately 19 to 38, This quantitative discrepancy does not, however, undermine the utility or validity of the proposed simulation system, for the following reasons. First, the primary objective of the simulation system is to predict the sequential variation of coloration in response to changes in oxide layer thickness, rather than to achieve exact chromatic reproduction. As demonstrated in Table 4, the system correctly reproduces the expected color order, namely green, violet, blue, brown, orange, and yellow. Second, the experimentally observed colors are influenced by multiple factors not accounted for in the ideal thin-film interference model. These include surface roughness, inhomogeneity of the oxide layer, non-stoichiometric oxide composition, as well as variations in illumination conditions and camera response during image acquisition. Collectively, these factors tend to reduce the saturation and lightness of the experimental colors, thereby contributing to the larger ΔE values. Third, the simulation system adopts a simplified optical model that assumes a perfectly smooth, uniform Fe_2O_3 layer with a constant refractive index. This simplification is intentionally employed to isolate the fundamental thin-film interference effect and to facilitate a clear understanding of the underlying coloration mechanism.

In the aforementioned data simulation process, the computation time for a single data point is within approximately 1 s, and remains below 2 s even when multiple interference orders are considered, demonstrating the system's capability for rapid color prediction and parameter scanning. Within the investigated thickness range (50-400 nm), the predicted color sequence remains stable, and minor perturbations in the refractive index (±0.05) and small variations in oxide film thickness (±2 nm) have little influence on the prediction results. Within 0-50 nm thickness the predicted color sequence remains relatively stable due to the dominance of a single interference wavelength, while for thicknesses exceeding 400 nm the color is influenced by three or more interference wavelengths, resulting in relatively weaker stability due to the superposition of multiple composite light components. In addition, the graphical interface allows intuitive parameter input and convenient visualization of simulation results, which improves the operational convenience of the system.

The proposed simulation system provides a convenient tool for predicting the relationship between oxide film thickness and interference color in laser-induced surface oxidation processes. This capability can assist in process optimization for applications such as laser color marking of stainless steel products, surface decorative processing, and anti-counterfeiting markings based on structural colors. By enabling rapid parameter evaluation and theoretical-experimental comparison, the system can reduce trial-and-error experiments during process development and provide useful guidance for industrial surface engineering applications.

7. Discussion

The results of this study demonstrate that the proposed thin-film interference model and simulation system can effectively predict the color evolution of laser-induced oxide layers on stainless steel surfaces. The simulated results show good agreement with the experimental observations, indicating the reliability of the proposed approach. Nevertheless, several limitations of the present study should be acknowledged.

The current optical model assumes that the oxide layer consists of a single material with uniform optical properties. In this study, the oxide layer was simplified as Fe_2O_3 for theoretical modeling. However, in practical laser oxidation processes on stainless steel, the oxide layer may consist of Fe-Cr composite oxides with varying compositions and refractive indices, which may introduce deviations between the predicted and actual optical responses.

Another limitation lies in the experimental parameter space investigated in this work. The experiments primarily focused on the influence of laser scanning speed on oxide film formation and the resulting interference colors. Other key laser processing parameters, such as laser power, pulse width, and repetition rate, were not independently analyzed, although they may significantly influence oxidation kinetics, and oxide layer thickness during laser processing.

In addition, the current interference model assumes an ideal smooth thin film. In practical laser processing, the surface may exhibit micro-scale roughness or morphological variations, which can introduce additional scattering effects and influence the observed interference colors.

Future studies will aim to improve the physical accuracy and applicability of the proposed model. Possible directions include incorporating refractive index data for multi-component oxide layers, extending the simulation framework to cover a broader range of laser processing parameters, and integrating surface morphology characterization to account for the influence of surface roughness on thin-film interference. Furthermore, the current prototype simulation system may be further developed into an industrial-level offline simulation tool to support parameter optimization and color prediction in laser surface engineering applications.

8. Conclusions

This study developed a Python-based simulation system for nanosecond laser-induced surface coloring (NLISC) of 304 stainless steel. The proposed system integrated the thin-film interference (TFI) theory and additive color mixing principles to achieve end-to-end simulation from oxide layer parameters to color block visualization, while incorporating an image region RGB value extraction module. This design not only provides theoretical insights but also demonstrates significant potential for industrial applications. The system can serve as an efficient virtual platform for process optimization, reducing trial-and-error costs and time while enabling precise and rapid customization of target colors. It holds considerable relevance for personalized color marking of consumer products, color coding and identification of industrial components, and artistic applications. Moreover, future work could extend the system to other metals or alloys, or adapt it to lasers of different wavelengths, by refining material parameters and the laser-material interaction models. The performed comparative analysis of experimentally observed and simulated color patches yielded the following conclusions:

1. By gradually reducing the laser spot overlap ratio (SOR) from 99.6% to 84% via scanning speed adjustment, we

obtained color blocks ranging from black and gray to green, violet, blue, brown, orange, and yellow. These results confirm that the TFI effect is the primary mechanism governing stainless steel surface coloration.

2. Comparison of the color transition sequences between simulated results and experimentally observed characteristic color patches demonstrated highly consistent ordering, validating the predictive reliability of the simulation system for NLISC-based oxide layer coloration of 304 stainless steel surfaces.
3. Within the CIELAB color space, additive color mixing principles implemented in the proposed Python-based software system successfully simulated composite coloration resulting from multiple interference wavelength superposition. This proved the CIE Lab* additive color model applicability to predicting interference-based chromatic effects.
4. The developed Python-based NLISC simulation system was applied to 304 stainless steel, proving that the TFI effect is the primary mechanism governing stainless steel surface coloration.

Acknowledgments

The authors acknowledge the experimental support from the Institute of Laser Engineering at the Beijing University of Technology, the Boyue Instruments (Shanghai) Company Limited and the financial support from the Natural Science Foundation of Hebei Province (F2024402016), the Hebei Key Laboratory of Optical Fiber Biosensing and Communication Devices (SZX2022010) and the Science and Technology Research and Development Plan of Handan Municipality, China (21422111223).

References

[1] Adams D P, Hodges V C, Hirschfeld D A, et al. Nanosecond pulsed laser irradiation of stainless steel 304L: Oxide growth and effects on underlying metal[J]. Materials Science and Engineering: A, 2013, 222: 1-8.

[2] Hongzhi G, Jianmei L, Mengyou H. Development and Expectation of Coloring Mechanism of Nanosecond Laser on Metal Surface[J]. Applied Laser, 2017, 37(05): 752-758.

[3] Zhenhua Z, Qingmao Z, Liang G. Research on Color Marking Mechanism based on Nanosecond Laser[J]. Applied Laser, 2016, 36(03): 331-336.

[4] Roozbahani H, Alizadeh M, Handroos H, et al. Color Laser Marking: Repeatability, Stability and Resistance Against Mechanical, Chemical and Environmental Effects[J]. IEEE Access, 2020, 8: 214196-214208.

[5] Unal F, Yavas A, Avinc O. Sustainability in textile design with laser technology[M]. Sustainability in the textile and apparel industries: Sustainable textiles, clothing design and repurposing. Springer. 2020: 263-287.

[6] Palneedi H, Park J H, Maurya D, et al. Laser irradiation of metal oxide films and nanostructures: applications and advances[J]. Advanced Materials, 2018, 30(14): 1705148.

[7] Bonse J, Kirner S V, Krüger J. Laser-induced periodic surface structures (LIPSS)[J]. Handbook of laser micro-and nano-engineering, 2020: 1-59.

[8] Guay J M, Calà Lesina A, Côté G, et al. Laser-induced plasmonic colours on metals[J]. Nature communications, 2017, 8(1): 16095.

[9] Hanzhang W, Yanrui Y, Zhiqiang D. Laser Coloring of Stainless Steel[J]. Laser & Optoelectronics Progress, 2023, 60(09): 342-347.

[10] Li Z, Zheng H, Teh K, et al. Analysis of oxide formation induced by UV laser coloration of stainless steel[J]. Applied Surface Science, 2009, 256(5): 1582-1588.

[11] Ma X, Nie X, Zhao J, et al. Effect of nanosecond pulsed laser parameters on the color making of 304 stainless steel[J]. Optics & Laser Technology, 2020, 126: 106104.

[12] Swayne M, Perumal G, Brabazon D. Mechanism for Control of Laser-Induced Stainless Steel Oxidation[J]. Advanced Materials Interfaces, 2024, 11(17): 2300991.

[13] Awasthi A, Kumar D, Marla D. Understanding the role of oxide layers on color generation and surface characteristics in nanosecond laser color marking of stainless steel[J]. Optics & Laser Technology, 2024, 171: 110469.

[14] Lazov L, Angelov N, Yankov E, et al. Influence of Laser Processing Parameters on Surface Roughness and Color Formation in the Marked Zone[J]. Materials, 2025, 18(21): 5037.

[15] Li S, Niu P, Yu X, Geng J, Shi L. Laser-Induced Metal Oxidation Coloring Technology: Principles, Processes, and Optimization (Invited). Laser & Optoelectronics Progress, 2025, 62(23): 2300006.

[16] Heavens O S. Optical properties of thin films[J]. Reports on Progress in Physics, 1960, 23(1): 1-65.

[17] Xue Y, Luo Z, Han S, et al. Mechanism analysis of laser coloring of Ti alloy by optical simulation[J]. Optik, 2022, 254: 168650.

[18] Xue Z, Wan X, Wang X, et al. Prediction model for laser marking colors based on color mixing[J]. Optics Express, 2024, 32(15): 26052-26068.

[19] Geng Y, Li J, Lu C. Experimental and numerical investigations on color stability of laser color marking[J]. Optics and Lasers in Engineering, 2022, 159: 107225.

[20] Cheng Z, Xue Y, Ju H. Chemical coloring on stainless steel by ultrasonic irradiation[J]. Ultrasonics Sonochemistry, 2018, 40: 558-566.

[21] Davidson K P, Littlefair G, Singamneni S. On the machinability of selective laser melted duplex stainless steels[J]. Materials and Manufacturing Processes, 2022, 37(12): 1446-1462.

[22] Liu H, Lin W, Hong M. Surface coloring by laser irradiation of solid substrates[J]. Apl Photonics, 2019, 4(5).

[23] Fang D, Jun-mao Q, Hao-hua D. Study on thermal physical properties of 304 stainless steel[C]//6th international symposium on high-temperature metallurgical processing. Cham: Springer International Publishing, 2015: 99-104.

[24] Bogaard R H, Desai P D, Li H H, et al. Thermophysical properties of stainless steels[J]. Thermochimica Acta, 1993, 218: 373-393.

[25] Lu Y, Shi X, Huang Z, et al. Nanosecond laser coloration on stainless steel surface[J]. Scientific reports, 2017, 7(1): 7092.

[26] Aziz M J. Film growth mechanisms in pulsed laser deposition[J]. Applied Physics A, 2008, 93(3): 579-587.

[27] Zhang L L, Yuan L M, Chen Y. Research of the process of laser-induced color marking on stainless steel[J]. Appl. Laser., 2017, 37(1): 115-121.

[28] Shepelin N A, Tehrani Z P, Ohannessian N, et al. A practical guide to pulsed laser deposition[J]. Chemical Society Reviews, 2023, 52(7): 2294-2321.

[29] Dubey A K, Yadava V. Laser beam machining—A review[J]. International Journal of Machine Tools and Manufacture, 2008, 48(6): 609-628.

[30] Harrick N J. Determination of refractive index and film thickness from interference fringes[J]. Applied optics, 1971, 10(10): 2344-2349.

[31] Peavy G M. Lasers and laser–tissue interaction[J]. Veterinary Clinics: Small Animal Practice, 2002, 32(3): 517-534.

[32] Klein G A, Meyrath T. Industrial color physics[M]. New York: Springer, 2010.

[33] Fairchild M D. CIE color appearance models[C]//9th Congress of the International Colour Association. SPIE, 2002, 4421: 550-553.

[34] Ohno Y. CIE fundamentals for color measurements[C]//NIP & Digital Fabrication Conference. Society of Imaging Science and Technology, 2000, 16: 540-545.

[35] Jing Q, Yang B L, Guan D W. Recent Progress in Surface Colorization Induced by Laser[J]. Surface Technology, 2021, 50(03): 16-29.

[36] Joerger R, Forcht K, Gombert A, et al. Influence of incoherent superposition of light on ellipsometric coefficients[J]. Applied optics, 1997, 36(1): 319-327.

[37] Jiang A, Westland S. The CIE System[J].Springer, Cham, 2024.

[38] Smith T, Guild J. The CIE colorimetric standards and their use[J]. Transactions of the optical society, 1931, 33(3): 73-134.

[39] Pridmore R W. Complementary colors theory of color vision: Physiology, color mixture, color constancy and color perception[J]. Color Research & Application, 2011, 36(6): 394-412.

[40] Chityala R, Pudipeddi S. Image processing and acquisition using Python[M]. Chapman and Hall/CRC, 2020.

[41] Van der Walt S, Schönberger J L, Nunez-Iglesias J, et al. scikit-image: image processing in Python[J]. PeerJ, 2014, 2: e453.

[42] Howse J. OpenCV computer vision with python[M]. UK: Packt Publishing Birmingham, 2013.

[43] Diamanti M V, Curto B D, Pedeferri M P. Interference colors of thin oxide layers on titanium[J]. Color Research & Application, 2008, 33(3): 221-228.

[44] Haynes W M. CRC handbook of chemistry and physics [M]. CRC press, 2016.

[45] Wu Z L, Reichling M, Hu X Q, et al. Absorption and thermal conductivity of oxide thin films measured by photothermal displacement and reflectance methods[J]. Applied optics, 1993, 32(28): 5660-5665.

[46] Zhang H, Li C, Zhang L, et al. Effect of laser pulse energy deposition method on nanosecond laser scanning ablation of SiCp/AA2024 composites[J]. Journal of Manufacturing Processes, 2022, 83: 695-704.